Journal of Energy Storage 72 (2023) 108636

Contents lists available at ScienceDirect

Journal of Energy Storage

journal homepage: www.elsevier.com/locate/est

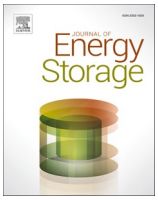

Research papers

Liquid immersion thermal management of lithium-ion batteries for electric vehicles: An experimental study

N.P. Williams *, D. Trimble, S.M. O'Shaughnessy

Department of Mechanical, Manufacturing, and Biomedical Engineering, Trinity College, University of Dublin, Ireland

ARTICLE INFO

Keywords:
Immersion cooling
Electric vehicles
Pool boiling
Dielectric liquid
Battery thermal management
Two-phase cooling

ABSTRACT

The thermal and electrical performance of lithium-ion batteries subjected to liquid immersion cooling conditions in a dielectric fluid has been experimentally investigated in this study. A single 26650 $LiFePO_4$ cylindrical cell is completely immersed in Novec 7000 and charged and discharged at onerous maximum rates of up to 4C and 10C, respectively, where C can be defined as the measure of the rate at which a cell is charged or discharged relative to its rated capacity. Immersion cooling offers high rates of heat transfer from the cell's surface, in particular when the saturation temperature of the fluid is exceeded, and two-phase conditions are established. At a preheated liquid pool temperature of 33 ± 0.5 °C for discharge rates ≥ 2C, subcooled boiling conditions develop, with the cell's temperature rise limited to 3.6 °C at the end of 10C discharge. Furthermore, for 4C charging under the same preheating conditions, the cell's temperature rise does not exceed 1 °C. Superior performance is observed under two-phase immersion cooling conditions in comparison to both single phase liquid immersion and natural convection air cooling for the same charge and discharge rates. Excellent thermal homogenisation across the cell is also determined, with a maximum axial temperature difference of 0.25 °C and 1 °C for 4C charging and 10C discharging respectively.

1. Introduction

Greater adoption of vehicles with low or zero carbon emissions such as electric vehicles (EVs) is required for various emission reduction targets to be reached. However, the properties of the lithium-ion cells from which their battery packs are comprised are highly temperature dependent, with reduced lifespan and performance outside the restrictive optimal operating temperature range of 25 °C to 40 °C [1]. Above this range, cells experience greater degradation from sources such as electrolyte decomposition and growth of the solid electrolyte interphase (SEI) layer which reduces cyclable lithium capacity [2]. At further elevated temperatures thermal runaway is of significant concern, in which exothermic cell decomposition can cause fire or explosion [3]. Issues are also faced below the optimum temperature range, in particular reduced charging rates, with the potential for lithium plating and ultimately short-circuiting to occur [4]. Furthermore, a temperature difference of no more than 5 °C between cells in a module configuration is considered acceptable [1] to mitigate against uneven degradation and detrimental cell imbalances. The environmental conditions which the EV will operate in must also be considered, particularly for extreme temperatures. The identification of fast charging, in which cells are charged to 80 % of their final capacity in 15 minutes [5], as a potential solution to range anxiety will place increased stress on the battery thermal management system (BTMS) due to power fade and accelerated degradation concerns [6].

Conventional forced convection air cooling BTMS have been shown to be incapable of maintaining an acceptable temperature distribution under high discharge rates or ambient conditions (> 50 °C) [7,8]. Despite several proposed methods to improve the performance of air cooling through module geometry optimisation [9–14] or flow redirection [15,16], the maximum cell temperature for many of these systems remained significantly in excess of 40 °C and was maintained below this limit only at low discharge rates or for modules consisting of low-capacity cells.

To fulfil the criterion of a minimal temperature variation throughout the module, the use of phase change material (PCM) for battery thermal management has been investigated by several researchers (*e.g.*, Refs. [17, 18]). PCM based systems utilise the material's high latent heat during phase change to absorb the heat generated by the surrounding cells, with paraffin wax commonly used. Despite the simplicity and

* Corresponding author.
E-mail address: nwilliam@tcd.ie (N.P. Williams).

https://doi.org/10.1016/j.est.2023.108636
Received 17 February 2023; Received in revised form 21 June 2023; Accepted 6 August 2023
Available online 16 August 2023
2352-152X/© 2023 The Author(s). Published by Elsevier Ltd. This is an open access article under the CC BY license (http://creativecommons.org/licenses/by/4.0/).

passive nature of these PCM systems, many of the materials studied possess phase change temperatures in excess of the maximum allowable cell temperature. Consequently, the latent heat transfer and high thermal homogeneity is available only at these elevated temperatures. For high discharge rates or under repeated cycling, complete phase change can occur, with the liquid phase offering little cooling due to its poor thermal conductivity. While the addition of high conductivity materials such as aluminium [19], copper foams [20–22], expanded graphite [23,24], and carbon fibre [25] to form composite matrices enhances the PCM's thermal properties, the performance of these systems remains poor under more onerous operating conditions.

The use of liquid (typically water or a water-glycol mixture) as the working fluid for battery thermal management has been found to offer increased heat transfer performance due to its superior heat capacity and thermal conductivity. Indirect contact systems have included cold plates containing minichannels [26–28] or microchannels [29–32], with the maximum cell temperature found to be dependent upon the flow rate of the working fluid, typically decreasing for greater flow rates. However, increased flow rates can have a deleterious effect on thermal homogeneity, increasing the thermal gradient along the channels and potentially exceeding the acceptable 5 °C limit. More uniform thermal conditions can be achieved for greater hydraulic diameters, the introduction of discontinuities to the channel walls, and increasing channel width from inlet to outlet. Improved thermal homogenisation has been observed in minichannel systems for working fluids with saturation temperatures in the cell optimum operating temperature range, such as the dielectric HFE 7000 [33] and the refrigerant R134a [34]. However, significant temperature excursions occurred for low inlet flow rates and high discharge rates due to complete vaporisation of the working fluid. Despite the greater performance illustrated by single and two-phase indirect contact forced convection systems in comparison to air cooled and PCM-based systems, the thermal contact resistance arising from the required separation of the working fluid and cells remains detrimental to heat transfer. Significant power consumption may also be associated with indirect contact cooling due to the complex ancillary cooling loops required to dissipate the generated heat.

The implementation of heat pipe BTMS has also been investigated, with their compact geometry and flexible structure an advantage to minimise system size. However, the start-up temperature of many of the heat pipes studied exceeded the desirable cell operating range [35] and would require integration in a thermal spreading device such as a cold plate, increasing system thermal resistance.

Direct contact liquid immersion cooling, in which the cell is immersed in an electrically non-conductive dielectric fluid, is receiving increased attention as a potential battery thermal management solution to mitigate against these issues, facilitating greater heat transfer and increased safety in a thermal runaway event. Reduced spatial and temporal cell temperature gradients have been observed for forced convection single phase direct contact liquid conditions, with superior performance in comparison to forced air convection conditions for prismatic cells illustrated by Chen and Li [36] and Sundin and Sponholtz [37] for complete immersion in a water-ethylene glycol mixture and the synthetic hydrocarbon dielectric fluid Ampcool AC-100, respectively. Acceptable thermal uniformity across a 20 Ah lithium iron phosphate ($LiFePO_4$ or LFP) prismatic pouch cell of less than 5 °C was observed numerically by Patil et al. [38] at a 3C discharge rate, where C represents the C rate, which can be defined as the measure of the rate at which a battery is charged or discharged relative to its rated capacity. They combined immersion of the cell body in mineral oil and forced convection air tab cooling. Liquid flow rates exceeding 0.0462 kg/s and inlet air velocities of 5 m/s at the tabs were required for the necessary thermal uniformity to be achieved in a full module design consisting of 14 cells. A 9.3 % decrease in the maximum cell temperature at 5C discharge was reported in comparison to the water-glycol cold plate module of Li et al. [39] for the same inlet flow rate and discharge conditions. Wang et al. [40] experimentally examined the performance of a module consisting of five 10 Ah pouch cells connected in parallel and immersed in mineral oil. Experiments were conducted for varying submergence depths and flow rates. For a discharge rate of 2C and complete immersion, a maximum temperature increase of 39.4 °C and temperature difference of 1.43 °C across the module was determined for the most optimal flow rate of 0.8 L/min.

Even greater rates of heat transfer and thermal homogenisation can be provided by two-phase direct contact immersion cooling through the latent heat of phase change; however, limited literature exists to date on this potential BTMS.

Hirano et al. [41] were among the first to investigate the suitability of this method, completely immersing a module consisting of ten 1 Ah prismatic cells in the dielectric fluid HFE 7000. The cells' surface temperatures were maintained at 35 °C ± 2.5 °C, with cell-to cell temperature variations of less than 1 °C for a total of 5 charge-discharge cycles at both 10C and 20C. Fluid preheating temperatures greater than 31 °C and pulsed charge-discharge (PCD) cycles at 5C for 90 s were required by van Gils et al. [42] to initiate nucleate boiling from a single 1 Ah 18500 cylindrical cell immersed in HFE 7000. Upon boiling incipience, near identical temperatures at the cell's electrodes were recorded, with a temperature difference of approximately 1 °C between the battery and surrounding fluid.

Single cell discharge in HFE 7000 was also investigated by Giammichele et al. [43] for a cylindrical 1.8 Ah 18650 $LiFePO_4$ cell, with nucleate boiling observed from the cell's electrodes for discharge rates above 2C and a fluid preheating temperature of 32 °C. The cell's surface temperature increase of 3.6 °C under two-phase conditions at 3C discharge was found to be approximately half of that under single phase conditions. Similar performance was determined by Li et al. [44] for a 3 Ah cylindrical 18650 cell immersed in the dielectric fluid SF33, with the average cell temperature maintained below 34.5 °C during 7C discharge under saturated boiling conditions.

The suitability of two-phase immersion cooling for thermal management during fast charging was later investigated by the same authors for the immersion of cylindrical cells of varying size and electrochemistry in the fluid SF33 [45]. The cell's temperature was held at approximately the fluid's saturation temperature of 33 °C during the constant current stage of 3C charging, with maximum temperature increases of 1.87 °C, 3.25 °C, and 3.38 °C determined for 18650 lithium titanium oxide (LTO), 26650 $LiFePO_4$, and 21700 lithium nickel manganese cobalt oxide (NMC) cylindrical cells, respectively.

The performance of a battery module under immersion cooling conditions was studied by Giammichele et al. [46] for a module consisting of nine cylindrical $LiFePO_4$ cells similar to those used in their previous work [43]. The module was configured in a 3 in series, 3 in parallel (3s, 3p) arrangement. For complete immersion in Novec (HFE) 7000 and at the greatest discharge rate investigated of 3C, a temperature rise of 10.69 °C was determined for the cell at the centre of the module, with minimal cell-to-cell temperature difference. In comparison, a temperature rise of 37.76 °C under natural convection air cooling conditions occurred under the same discharge rate.

Flow boiling arrangements for battery thermal management have also been examined, with Wang and Wu [47] both numerically and experimentally investigating the performance of a module consisting of sixty 3.2 Ah NMC 811 cylindrical cells in a 5s, 12p arrangement and utilising HFE 7000 as the working fluid. A maximum cell temperature of 37.2 °C and cell-to-cell temperature difference of 3.71 °C was reported under 5C discharge. The inlet velocity was found to dictate the intensity of the boiling, with increasing velocities reducing the maximum cell temperature and improving thermal homogenisation across the module due to low vapour fraction and bubble coalescence.

Wu et al. [48] implemented a flow boiling system for a single 20 Ah $LiFePO_4$ pouch cell to prevent the accumulation of low conductivity HFE 7000 vapour on the cell's surface during 2C charge-discharge cycling and non-replenishing pool boiling conditions. For coolant volumetric flow rates from 6.8 mL/min to 25.5 mL/min, the cell temperature was

maintained below 35 °C under cycling conditions; however, increased temperature variations across the surface were observed as boiling was supressed close to the inlet. To address this, the authors developed an intermittent flow mode, in which a total coolant volume of 24 mL was added at hourly intervals at a rate of 12 mL/min, with a maximum temperature of 35 °C and temperature difference of less than 2 °C across the cell.

As part of their work on a proposed hybrid electric vehicle (HEV) propulsion system, in which the fuel for the internal combustion engine (ICE) could be vaporised by the heat generated by the battery module, Al-Zareer et al. performed several numerical pool boiling studies examining the thermal performance of both cylindrical and prismatic cells under immersion cooling conditions. These combined battery thermal management-ICE fuels included propane [49], ammonia [50,51] and the refrigerant R143a [52]. A coupled 1D electrochemical and 3D lumped heat and mass transfer model was developed, in which the cell heat generation rate was determined from the electrochemical model based on the work of Doyle et al. [53] and a nucleate boiling correlation was applied to the liquid pool for an incipience temperature of 5 °C. Lower maximum cell temperatures coupled with improved thermal homogeneity were observed for increasing immersion pool heights as a greater cell surface area was subjected to boiling heat transfer rather than low conductivity vapour. For partial immersion pool heights of up to 30 % of the total cell height, the temperature difference between cells remained above the allowable limit. Complete immersion conditions were found to offer the lowest cell temperatures and greatest thermal homogeneity. The influence of the cylindrical cell spacing on module performance was also investigated for spacings of 0.5R to 2R, where R is the cell's radius. Lower maximum cell temperatures were observed for increasing spacing, with greater thermal homogeneity exhibited for more closely packed cells as the vapour volume fraction approached unity more rapidly, albeit this came at the expense of higher cell temperatures.

Zhuo et al. [54] proposed a heat pipe-immersion cooling BTMS in which a total of fourteen 60 Ah NMC pouch cells were arranged in a module format and immersed in the dielectric fluid Novec 649, with porous polyurethane mats placed between the cells to promote the upward movement of the vapour. Sixty heat pipes with acetone as the working fluid were used to condense the vapour produced, with the evaporator sections of the heat pipes placed above the liquid pool. Aluminium fins were attached to the condenser sections housed outside the battery module to increase heat transfer to the ambient air. The module was subjected to cycling typically encountered by a hybrid tram system, with a maximum discharge rate per cell of 2.5C. Under the most onerous conditions, a maximum cell temperature of 46.5 ± 0.2 °C was maintained under ambient temperature conditions of 28 °C. Under a constant current discharge rate of 2C per cell, a maximum cell temperature of 48 °C was reached, with a temperature gradient of 2 °C between the cells.

1.1. Research aim

This study aims to ascertain the effectiveness of immersion cooling of lithium-ion cells by experimentally examining the thermal and electrical response of a single cylindrical lithium-ion cell during charging and discharging. Specifically, the study examines the cell voltage and current profiles, and the cell surface temperature at five locations.

A purpose-built test chamber is constructed, in which the cell is completely immersed in a dielectric fluid with a saturation temperature in the required lithium-ion cell operating temperature range. The fluid is preheated to a temperature conducive to the establishment of two-phase cooling during cell charge/discharge. First, the performance of the cell under constant current discharge rates of up to 10C is investigated. The proposed method is assessed with regard to the cell's maximum temperature and thermal gradient. The measured performance during discharge of the two-phase immersion cooling method is subsequently compared to both single phase immersion cooling using the same liquid and natural convection air cooling conditions. The behaviour of the cell under liquid immersion cooling conditions at charging rates of up to 4C, considered fast charging, is also investigated.

A number of pertinent studies investigating liquid immersion cooling BTMS are summarised in Table 1. To the authors' knowledge, the current study presents the most extensive set of results reported for the charging and discharging performance of this cell type under liquid immersion cooling conditions in any dielectric fluid.

2. Experimental method

2.1. Test chamber

The test section consists of a central chamber of internal dimensions 0.1 m × 0.1 m × 0.2 m constructed from welded 316L stainless steel plates each of 0.01 m thickness, as illustrated in Fig. 1. Machined 316L stainless steel flanges are secured to the chamber's faces *via* M5 bolts, with the upper and lower flanges sealed by Viton (FKM) rubber O-rings of 0.025 m^2 cross sectional area and the vertical flanges sealed by 0.0015 m thick Viton rubber gaskets. These were chosen for their material compatibility with the working fluid which is known to extract plasticisers from polymer materials and can lead to contamination. All required connections to the cell are made through cable glands with Viton seals secured to the external flanges, with polycarbonate viewing windows located in two opposing flanges to allow for inspection of the cell during the charging and discharging processes. The cell is orientated such that the positive electrode is located closest to the liquid pool's surface.

The cell is completely immersed in an initially quiescent liquid pool which has a volume of approximately 1 L. Vapour produced during the liquid's phase change is condensed by a copper coil of 8 mm outer

Table 1
Summary of liquid immersion cooling BTMS studies.

Cell type	Fluid (boiling point)	Discharge/ charge rate	Maximum temperature rise [°C]
1 Ah prismatic pouch (10 cell module) [41]	Novec (HFE) 7000 (34 °C)	10C discharge	5.7
	Novec 649 (49 °C)		7.4
1 Ah Sony cylindrical 18500 [42]	HFE 7000 (34 °C)	5C charge-discharge pulse	1.5
1.8 Ah ENERpower cylindrical 18650 LFP [43]		2C discharge	3.3
		3C discharge	3.6
20 Ah prismatic pouch LFP [48]		4C discharge	10
3 Ah Sony cylindrical 18650 [44]	SF33 (33.4 °C)	7C discharge	4.5
2.5 Ah cylindrical 26650 LFP [45]		3C charge	3.3
3 Ah Sony cylindrical 18650 (21 cell module) [55]	SF49 (49 °C)	1C charge	4
		2C charge	4.2
		3C charge	4.6
		4C charge	4.8
3.5 Ah LG Chem cylindrical 18650 NMC (16 cell module) [56]	E5-TM 410 (–)	1C discharge	7.4
		2C discharge	17.3
		3C discharge	29.1
		4C discharge	35.2
3 Ah Murata cylindrical 18650 (8 cell module) [57]	CFX70 (70.6 °C)	10C charge-discharge pulse	4
68 Ah Samsung prismatic hard shell [37]	Ampcool AC-100 (–)	1C discharge	2.1
		2C discharge	4.8
20 Ah A123 prismatic pouch LFP [38]	Mineral oil (–)	1C discharge	7
		2C discharge	15
		3C discharge	20

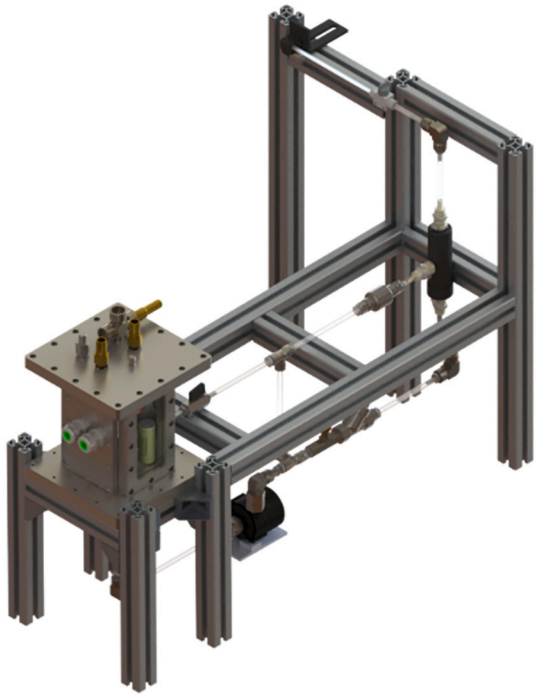

Fig. 1. 3D computer aided design (CAD) render of experimental set-up.

diameter located above the liquid pool. Water at a constant temperature of 15 °C and a fixed flow rate of approximately 3 L/min (5×10^{-5} m^3/s) is supplied to the coil by a Thermo Scientific Accel LC 500 recirculating chiller which can control the temperature of the coolant to ±0.1 °C. The flow rate is monitored by a Gems Sensors FT-110 Series turbine flow meter with a measurement range of 1 L/min to 15 L/min. The internal arrangement of the test chamber including connections to the cell is illustrated in Fig. 2 (a), with a schematic of the complete experimental set-up presented in Fig. 2 (b).

2.2. $LiFePO_4$ lithium-ion cell details

The performance of a single LithiumWerks ANR26650M1B 26650 $LiFePO_4$ cylindrical cell is investigated in this study. Electrical and thermophysical cell properties are outlined in Table 2. The cell is 25.96 ± 0.5 mm in diameter, 65.15 ± 0.5 mm in length, and has a mass of 76 ± 1.0 g. The heat generation rate of lithium-ion cells is time-dependent, and dictated by their temperature, state of charge, and the current either supplied or drawn during operation. Indicative heat generation rates can

Table 2
Electrical and thermophysical properties of the LithiumWerks ANR26650M1B $LiFePO_4$ cell.

Property	Value	Unit
Nominal capacity	2.5	Ah
Nominal voltage	3.3	V
Maximum continuous discharge current	50 (20C)	A
Maximum continuous charge current	10 (4C)	A
Density	2047 [59]	kg/m^3
Specific heat capacity	1605 ± 80 [60]	J/kgK
Axial thermal conductivity	32 ± 1.6 [60]	W/mK
Radial thermal conductivity	0.15 ± 0.01 [60]	W/mK

be determined from previous studies on the same lithium-ion cell under natural convection air cooling conditions [58], varying from approximately 3 W to 28 W at the end of 1C and 10C discharge, respectively.

Nickel tabs of 0.15 mm thickness were spot-welded to the cell's electrodes by the cell's supplier. The required electrical connections are made using spade terminals and 6 mm^2 tri-rated cable. All cabling within the test chamber is covered in suitable heat shrink material for increased material compatibility with the working fluid.

The cell's parameters can be expressed in terms of the state of charge (SOC) which describes the cell's charge level with respect to its capacity, and is defined as in Eq. (1):

$$SOC(t) = SOC(t_0) + \int_0^t \frac{I}{C_{cell}} dt \tag{1}$$

Here t is the elapsed time during the charge/discharge process in seconds, I is the current either provided to or drawn from the cell in Amperes and C_{cell} is the cell's nominal capacity in Ampere hours (Ah). During the discharge process, the cell's parameters are often expressed with respect to the depth of discharge (DOD), which is the converse of SOC, and varies from values of 0 (fully charged) to 1 (fully depleted):

$$DOD(t) = 1 - SOC(t) \tag{2}$$

Bernardi et al. [61] performed a general energy balance on a complete lithium-ion cell to describe the internal heat generation during the charging/discharging process, which can be expressed in a simplified form as the sum of the irreversible (Q_{irr}) and reversible (Q_{rev}) heat generation rates:

$$Q_{cell} = Q_{irr} + Q_{rev} \tag{3}$$

The irreversible heat generation rate is determined as the product of the charge/discharge current and the cell's overpotential η, which arises as a result of ohmic losses and mass transfer limitations within the cell [62]. For discharge, the irreversible heat generation rate can be expressed as in Eq. (4) where U and V are the cell's open circuit voltage (OCV) and terminal voltage respectively:

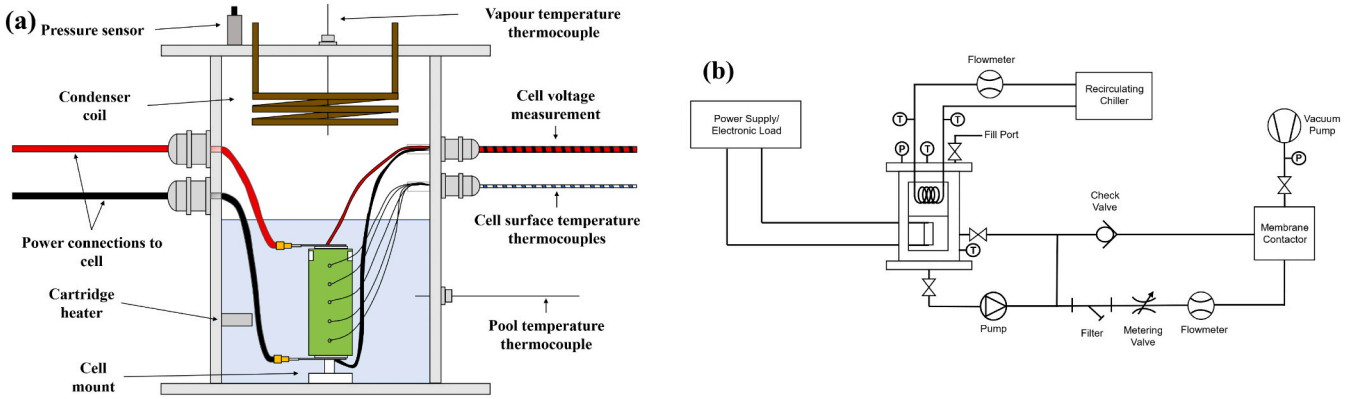

Fig. 2. Schematics of (a) the internal arrangement of the cell within the test chamber and (b) the experimental set-up including the degassing loop and electrical connections.

$$Q_{irr,dis} = I\eta_{dis} = I(U - V) \quad (4)$$

For the charging process, the voltage at the cell's terminals is greater than the OCV for a given SOC. Therefore, the irreversible heat generation can be expressed as:

$$Q_{irr,char} = I\eta_{char} = I(V - U) \quad (5)$$

The reversible heat is dictated by the cell's entropic heat coefficient $\frac{dU}{dT}$, which describes the behaviour of the cell's OCV at a given SOC with respect to the average cell temperature T in K.

$$Q_{rev} = IT\frac{dU}{dT} \quad (6)$$

2.3. Working fluid

The cell is completely immersed in 3M's Novec 7000 engineered fluid, a hydrofluoroether (HFE) dielectric liquid chosen for its desirable saturation temperature of 34 °C which is within the required cell optimal operating range. Furthermore, this fluid has no flash point and thus provides increased safety in the event of thermal runaway. Some properties of the working fluid are detailed further in Table 3.

As the heat generation rate of lithium-ion cells is known to be relatively low due to their high efficiency in converting the stored electrochemical energy to electrical energy, an auxiliary cartridge heater is located in the liquid pool to raise the bulk fluid temperature to a value conducive for two-phase heat transfer conditions to be established during cell charging and discharging. For results presented in Sections 3.1.1 and 3.2.1 of this study, the bulk fluid was preheated to a setpoint temperature of 33 ± 0.5 °C.

2.4. Data acquisition

The cell's voltage is measured directly using a National Instruments (NI) 9215 data acquisition module (DAQ), with an uncertainty of 0.02 % of the reading at room temperature in the range of ±10.4 V. The current either drawn from or supplied to the cell during operation is indirectly measured using a Honeywell CSLA1CF open loop current transformer which has a range of 0 to 100 A. The voltage output proportional to the current flowing through the transformer is recorded using an NI 9201 DAQ, which has an uncertainty of 0.04 % of the reading at room temperature in the range of ±10.53 V.

The cell's surface temperature as well as the temperature difference across the cell is determined from five T-type thermocouples of 2×10^{-4} m diameter. The thermocouples are attached to the cell's surface using high conductivity thermal adhesive (OMEGABOND 101) at an axial spacing of 11 mm. T-type thermocouple probes, each of 1.5×10^{-3} m diameter, are used to measure the liquid pool and vapour temperatures. All temperatures are recorded using an NI 9213 DAQ with an uncertainty of 0.02 °C. The instantaneous readings of the five surface mounted thermocouples are averaged to determine the cell's surface averaged temperature $T_{surf,avg}$.

The saturation conditions of the working fluid within the chamber are monitored by an Omega PX61C1 pressure transducer with a measurement range of 0 to 50 psi (0 to 345 kPa). The voltage output from this sensor is recorded using an NI 9219 DAQ which has an uncertainty of 0.1 % of the reading at room temperature in the range of ±0.125 V.

Table 3
Thermophysical and electrical properties of 3M Novec 7000 at 25 °C.

Property	Value	Unit
Boiling point	34	°C
Liquid density	1400	kg/m^3
Kinematic viscosity	3.2×10^{-7}	m^2/s
Specific heat capacity	1300	J/kgK
Thermal conductivity	0.075	W/mK
Latent heat of vaporisation	142	kJ/kg
Surface tension	0.0124	N/m
Dielectric strength	40	kV

2.5. Uncertainty reporting

An uncertainty analysis was performed to determine the uncertainty in the measured and calculated parameters. The uncertainty of directly measured parameters including the cell's voltage is determined from the measurement, or Type A, uncertainty, and instrument uncertainty. For the thermocouple and current transformer measurements, the precision error for the least-squares fit from their calibration at a 95 % confidence level is also considered [63]. All uncertainties are reported in Table 4.

2.6. Cell charging procedure

The cell is charged under constant current-constant voltage (CC-CV) conditions using a programmable Elektro-Automatik EA-PS 8360-10 T power supply, which has accuracies for current and voltage setpoints of ±0.02 A and ±0.72 V respectively. The charging process is controlled through a bespoke NI LabVIEW program which also records all measured parameters. First, the cell is discharged at a rate of 1C until the cut-off voltage of 2 V is reached, indicating the cell is completely depleted and at a SOC of 0. The cell is allowed to rest for a period of 1 h post-discharging for the OCV to settle. This also ensures that all charging commences from a similar initial OCV. During the constant current stage of the charging process, the desired current is supplied while the voltage across the cell's terminals is allowed to increase until the charge voltage limit of 3.6 V is reached. The constant voltage stage is subsequently initiated, in which this voltage limit is maintained across the cell electrodes while the current from the power supply decays. Charging ceases and the cell is considered fully charged when the current supplied reaches the cut-off value of 0.125 A as defined by the cell's manufacturer.

Due to limitations in the power supply equipment, the correct voltage limit of 3.6 V is supplied during the CV stage of charging; however, the cell experiences a drop in the voltage across its terminals during the power supply's switching event between its constant current and constant voltage output modes. This voltage subsequently recovers to the charge limit.

2.7. Cell discharging procedure

Prior to constant current discharging, the cell is charged under CC-CV conditions at a rate of 1C and in a similar manner to the charging procedure, allowed to rest for a period of 1 h post-charging for the OCV to settle. The cell is subsequently discharged at the required current using a programmable Elektro-Automatik EA-EL 9080-45T electronic load, with a current accuracy of ±0.09 A. The discharge process ceases when the cut-off voltage of 2 V is measured across the cell's terminals. The discharging process is also controlled through a bespoke NI LabVIEW program.

3. Results and discussion

In this section, several figures plot the surface temperature rise of the cell, described by Eq. (7) as the difference between the average surface temperature during charge or discharge and the initial average surface temperature.

Table 4
Measurement uncertainties.

Measurement	Uncertainty	Unit
Temperature	±0.59	°C
Voltage	±0.0016	V
Current	±0.068	A

$$\Delta T = T_{surf,avg}(t) - T_{surf,avg}(t_0) \quad (7)$$

3.1. Cell discharging

3.1.1. Preheated immersion cooling in HFE 7000

Fig. 3 (a) presents ΔT for preheated immersion cooling in (Novec) HFE 7000 and constant current discharge rates of 1C to 10C. The corresponding voltage profiles are provided in Fig. 3 (b). Increasing cell average surface temperatures are observed for all discharge rates, with greater temperature rises for higher discharge rates. This occurs as greater irreversible heat generation rates are produced as a result of the development of more significant overpotentials η within the cell, coupled with the increased current. The temperature profiles of the cell appear to be dictated by their corresponding voltage profiles, with the initial sharp temperature rise a result of the rapid decline in voltage at the beginning of the discharge process due to high internal resistance. For the lower discharge rates examined of 1C to 3C, the cell's temperature remains somewhat constant for DOD values of 0.2 to 0.9, in response to the cell's relatively 'flat' voltage profile which is characteristic of the $LiFePO_4$ chemistry. For discharge rates of 4C and above, the cell's decreasing voltage profile is more pronounced and accompanied by a more distinct surface temperature increase throughout the discharge. As the completely discharged state at DOD = 1 is approached, the cell's voltage rapidly drops in response to its increasing internal resistance, generating greater irreversible heat. This rapid drop occurs earlier in the discharge process for increasing C rates, initiating at DOD = 0.95 and DOD = 0.85 for rates of 1C and 10C respectively. The suitability of two-phase immersion for battery thermal management is clearly evident, as the average cell temperature is maintained within the desirable operating limit of 40 °C at all discharge rates investigated. A maximum temperature rise of 3.6 °C is determined under the most onerous discharge conditions of 10C, corresponding to an average cell surface temperature of 35.9 °C.

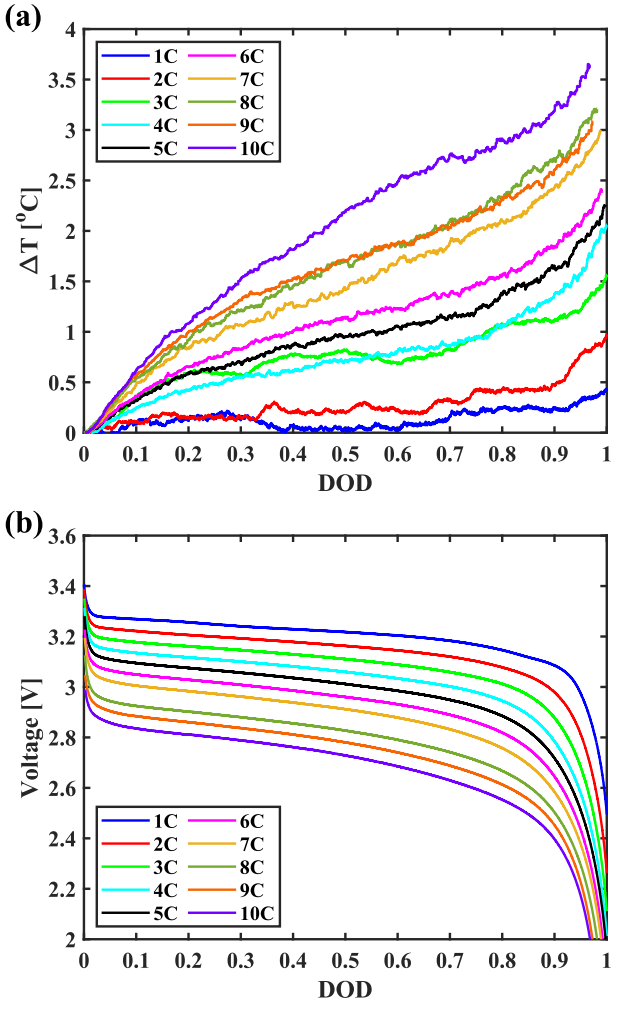

Fig. 3. (a) Average surface temperature rise of the ANR26650M1B cell under constant current discharge rates of 1C – 10C with respect to initial cell temperature for preheated immersion conditions, and (b) corresponding voltage profiles of the cell.

For the lowest discharge rate of 1C, the cell's average surface temperature does not exceed the saturation temperature of the fluid, with single phase natural convection remaining the dominant mechanism of heat transfer.

Subcooled boiling conditions are established for discharge rates $\geq$ 2C as while the cell's temperature rises above the fluid's boiling point, the bulk liquid temperature remains below the saturation temperature due to its low thermal conductivity. The latent heat of phase change maintains a relatively constant cell average temperature profile under preheated conditions during the 'flat' stage of the voltage profile between DOD values of 0.2 and 0.9 as the saturation temperature is exceeded.

The nucleation of vapour bubbles is not observed until a DOD $\approx$ 0.8 is reached under 4C discharge. These vapour bubbles grow and coalesce on the cell's lower (negative) electrode before departing, enhancing heat transfer by disturbing the cell's thermal boundary layer as they rise through the liquid pool. This behaviour has also been observed in previous studies on lithium-ion battery immersion cooling [43,44]. As the discharge process progresses, vapour bubbles of smaller diameter subsequently develop on the upper (positive) electrode surface, first observed at the end of 4C discharge at a DOD $\approx$ 0.98. These bubbles depart the surface more frequently in comparison to the lower electrode, with the spot-welded interface between the nickel tab and upper electrode observed to act as a nucleation site for their development. The intensity of the boiling process is noted to increase for greater discharge rates, developing on both upper and lower electrode surfaces at lower DOD values and with increasing bubble departure frequency.

The trends of the cell's voltage profiles of Fig. 3 (b) for all discharge rates investigated are consistent and show good agreement with those provided by the cell's manufacturer for constant current discharge under natural convective air cooling conditions at 25 °C [64]. Decreasing cell voltages, in particular at the start of discharge, are observed for increasing C rates as more substantial overpotentials occur within the cell. The cut-off voltage is noted to be reached at decreasing DOD values for the higher C rates investigated, as greater losses arise within the cell due to increased resistance to the lithium-ion transfer process, reducing the available capacity [65].

3.1.2. Single phase immersion cooling in HFE 7000

To compare the performance of preheated immersion cooling, Fig. 4 (a) plots the cell average surface temperature rise against those obtained for single phase liquid immersion in (Novec) HFE 7000. For discharge rates of 1C to 4C, greater average surface temperature increases are observed under single phase liquid immersion conditions in comparison to preheated immersion cooling conditions, for bulk liquid temperatures between 18 °C and 21 °C. A consistent and more pronounced surface temperature rise is observed throughout the discharge process under single phase liquid immersion conditions compared to preheated immersion cooling. For 4C discharge, a temperature rise of 6.8 °C is determined under single phase liquid immersion conditions, while a rise of only 2.1 °C occurs under preheated conditions, illustrating the superior performance of two-phase immersion cooling. These temperature rises correspond to average cell surface temperatures of 27.3 °C and 34.7 °C respectively.

3.1.3. Natural convection air cooling

Further comparison of preheated conditions can be performed against natural convection air cooling conditions in the same

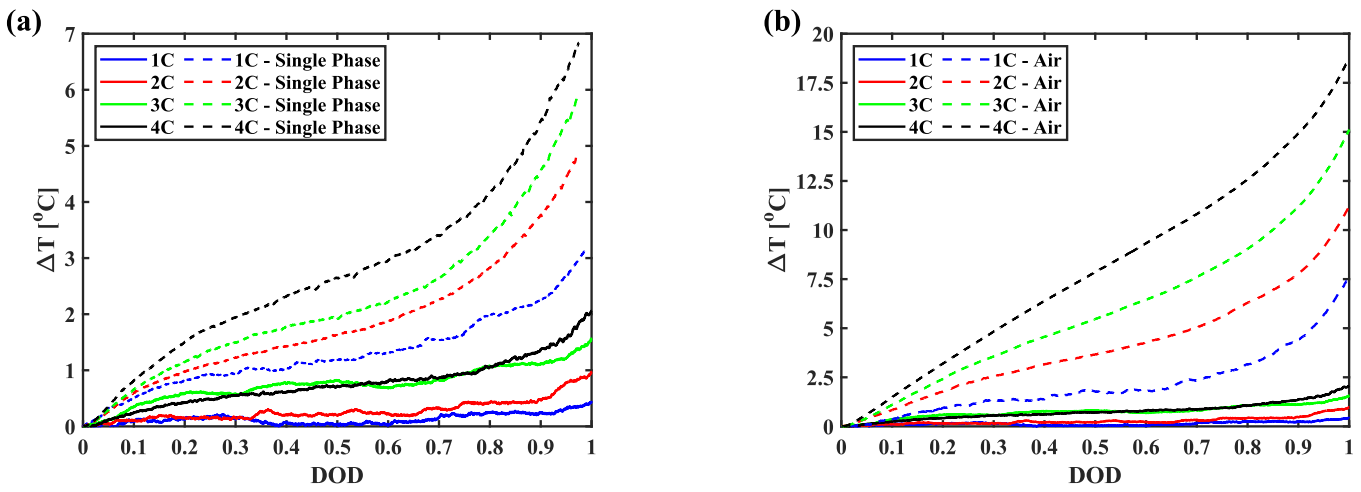

Fig. 4. Temperature rise of the ANR26650M1B cell under (a) single phase liquid immersion cooling and (b) natural convection air cooling, in comparison to liquid preheating (solid lines) for constant current discharge rates of 1C – 4C.

experimental set-up for bulk air temperatures between 19 °C and 21 °C. Good agreement was found between the maximum temperature rise under natural convection air cooling conditions in Fig. 4 (b) and the work of Giammichele et al. [58] and Chiew et al. [66] for the discharge of similar 26650 cylindrical $LiFePO_4$ cells. The average surface temperature rise of 7.4 °C during 1C discharge in stagnant air exceeds that measured for all discharge rates investigated under both preheated and single phase liquid immersion cooling in (Novec) HFE 7000. A cell average surface temperature of 39.9 °C is reached under natural convection air cooling at the end of 4C discharge, representing a temperature rise of approximately 19 °C. The unsuitability of natural convection air cooling for battery thermal management is clearly illustrated, with the cell likely to exceed the required operating limit for discharge rates of 5C and above.

As the heat generated by a lithium-ion cell is dependent upon factors such as the electrochemistry, capacity, charge/discharge rate, geometry, state of charge and environmental conditions, direct comparison with other BTMS studies utilising different cell types can prove difficult. However, to indicate the potential performance enhancement offered by immersion cooling, several pertinent PCM and liquid based BTMS studies on cells whose properties most closely align with those investigated in the current study are summarised in Table 5.

Improved performance is observed for both the single phase and two-phase immersion cooling conditions of this study in comparison to these alternative BTMS, with significantly lower cell temperature rises for similar discharge rates.

3.1.4. Cell temperature gradient comparisons

During operation, temperature differences develop within lithium-ion cells which increase in intensity with charge/discharge current and can lead to accelerated aging through reduced capacity as well as lithium plating. It is therefore desirable for a battery thermal management solution to minimise these cell temperature gradients. Fig. 5 illustrates the maximum temperature difference between any two thermocouple measurements on the cell surface for selected discharge rates of 2C to 10C under preheated immersion conditions. At 2C, as the heat generation rate is low due to the cell's high electrical efficiency, the surface temperature remains relatively uniform with a temperature difference of approximately 0.1 °C established across the cell at the end of discharge. More significant temperature differences are experienced by the cell for greater discharge rates as more intense electrochemical reactions occur. A maximum point-to-point surface temperature difference of approximately 1.1 °C is determined under the most onerous discharge conditions of 10C, in this case between the thermocouples located closest to the lower and upper electrodes as lithium-ions are transferred from the anode to cathode during the discharge process. For comparison, under otherwise the same test conditions, maximum axial temperature differences under 4C discharge of 0.9 °C for both single phase liquid cooling and natural convection air cooling are obtained.

Table 5
Summary of BTMS studies on single cylindrical cells.

Cell type	BTMS	Discharge rate	Maximum temperature rise [°C]
2.5 Ah Samsung INR18650–25R cylindrical NCA [67]	Aluminium fin enhanced PCM	1C	4.1
		2C	9.2
26650 cylindrical LFP [68]	PCM-graphite matrix	5C	18
2.5 Ah A123 26650 cylindrical LFP [69]	PCM only	2C	8.3
2 Ah 18650 cylindrical NMC [70]	Indirect contact water cooling tubes	0.5C	3.6
		1C	8.7
		3C	9.1

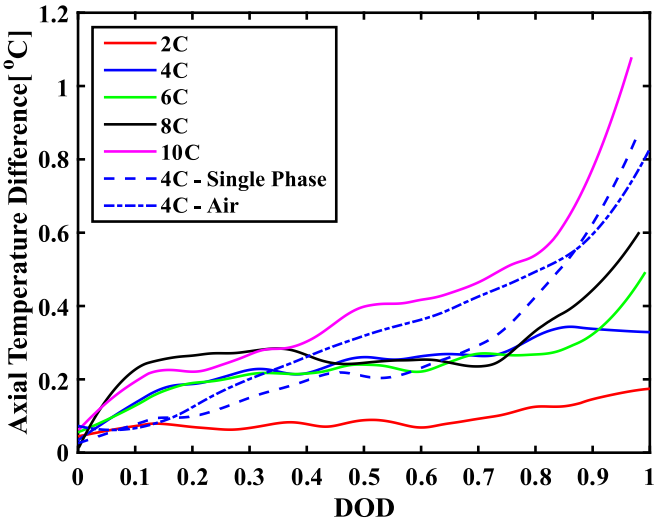

Fig. 5. Maximum measured cell surface temperature difference across the ANR26650M1B cell during discharge for preheated liquid immersion, single phase liquid immersion, and natural convection air cooling conditions.

3.2. Cell charging

3.2.1. Preheated immersion cooling in HFE 7000

The average surface temperature change of the cell under preheated immersion cooling in (Novec) HFE 7000 is illustrated in Fig. 6 as a function of SOC for CC-CV charging rates of 1C to 4C. As before, the cell temperatures are presented with respect to their initial temperature upon commencement of charging, as described in Eq. (7). Corresponding voltage and current profiles are also provided in Fig. 7 (a) and (b) respectively.

The cell experiences an initial decrease in average temperature when charging commences as the reversible heat generation is of significance at low SOC. The entropic heat coefficient $\frac{dU}{dT}$ of the cell is negative at the beginning of the charging process [71], with the reversible heat generation, and by extension the overall heat generation, subsequently endothermic to enable the cell's electrochemical reactions to occur. At greater charge rates the reversible heat is less influential as the cell's heat generation (Q_{cell}) is dominated by the irreversible heat. This leads to successively smaller reductions in cell temperature at the beginning of charging. The average surface temperature of the cell rises from an SOC of approximately 0.03 onwards and continues to increase throughout the CC stage of the charging process, with more rapid temperature rises for greater charging currents due to the cell's higher irreversible heat generation. As illustrated in Fig. 7 (a), higher cell voltages are reached more quickly as the C rate increases, as more significant overpotentials are required to supply the charging current. An average surface temperature rise of approximately 1 °C is determined at the end of the CC stage for both 3C and 4C charging rates, despite the greater heat generation rate at the 4C rate. This is attributed to the shorter duration CC stage for 4C charging as the cell's voltage limit is reached more quickly at an SOC of 0.83. The heat generation rate subsequently falls below that during 3C charging, for which the voltage limit is not reached until an SOC of 0.93.

It is noted that the dominant mechanism of heat transfer during charging under the preheated liquid immersion conditions investigated remains single phase convection, with the fluid's saturation temperature exceeded only at the end of the CC stage at the 3C charging rate. Furthermore, the lowest charging time required for the cell to reach an SOC of 1 is observed under preheated immersion conditions as the efficiency of the cell's electrochemical reactions are improved at elevated temperatures.

Upon initiation of the CV stage of the charging process, a decrease in the cell's voltage is observed, which arises due to a limitation of the equipment used. During the power supply's switching event from its constant current mode to the constant voltage mode when the charging voltage limit of 3.6 V is reached, there is a slight decrease in output voltage to match this limit. There is a corresponding decrease in the cell's voltage, which subsequently recovers to the maximum charge limit during the CV stage as can be observed in Fig. 7 (a).

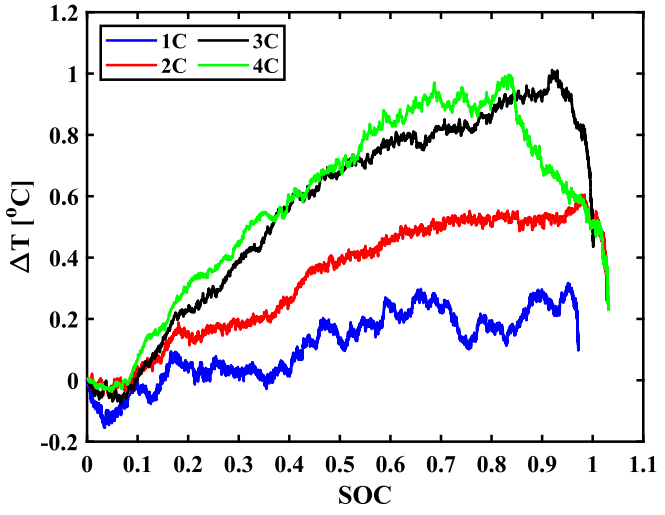

Fig. 6. Average surface temperature change of the ANR26650M1B cell under CC-CV charge rates of 1C – 4C with respect to initial cell temperature for preheated immersion conditions.

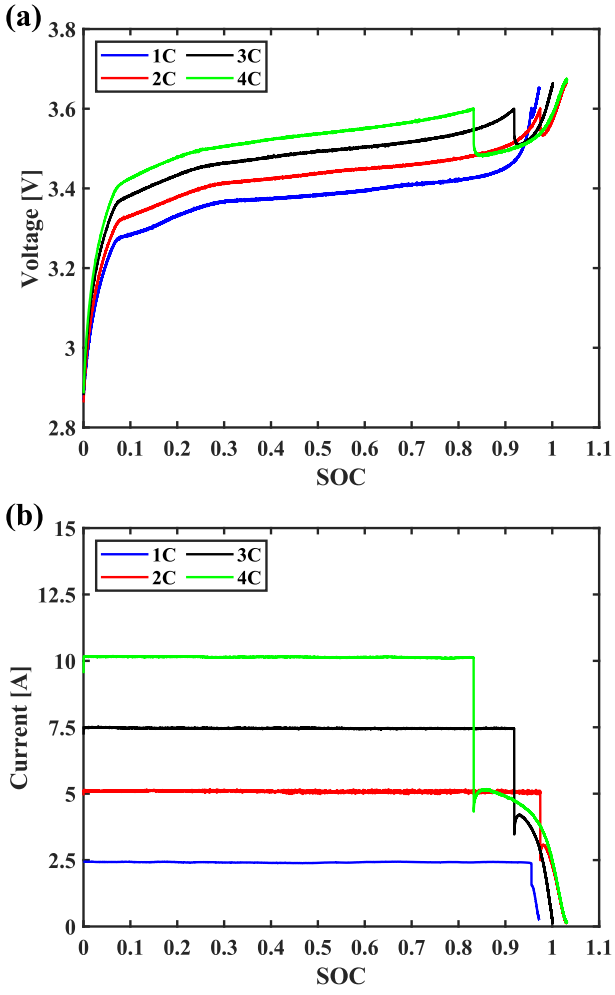

Fig. 7. (a) Voltage profiles of the ANR26650M1B cell under CC-CV charge rates of 1C – 4C for preheated immersion conditions, and (b) corresponding current profiles of the cell.

The current supplied to the cell falls significantly during the CV stage, as illustrated in Fig. 7 (b), and is accompanied by a decrease in the cell's temperature as the irreversible heat generation rate Q_{irr} is reduced. The exceedance of an SOC value of 1 is attributed to the increase in charge current in response to the drop in voltage after the power supply's CC to CV switching event. The current subsequently decays as the voltage recovers to the charging limit, with greater recovery times observed for increasing charging rates.

Similar behaviour at the charging rate of 3C was observed by Li et al. [45] for the same 26650 $LiFePO_4$ cylindrical cell immersed in the dielectric fluid SF33, which has comparable thermal properties to (Novec) HFE 7000. Good agreement was found for the total charging time, as in Fig. 8 (a), with the CC stage observed to end at an SOC of approximately 0.92 in this study, in comparison to a value of 0.9 as reported by Li et al. [45]. The previously discussed drop in voltage during the CV switching event is clearly evident. However, as illustrated in Fig. 8 (b), a greater cell temperature increase was determined by Li et al. [45] throughout the charging process as the cell was immersed in a significantly lower volume of fluid.

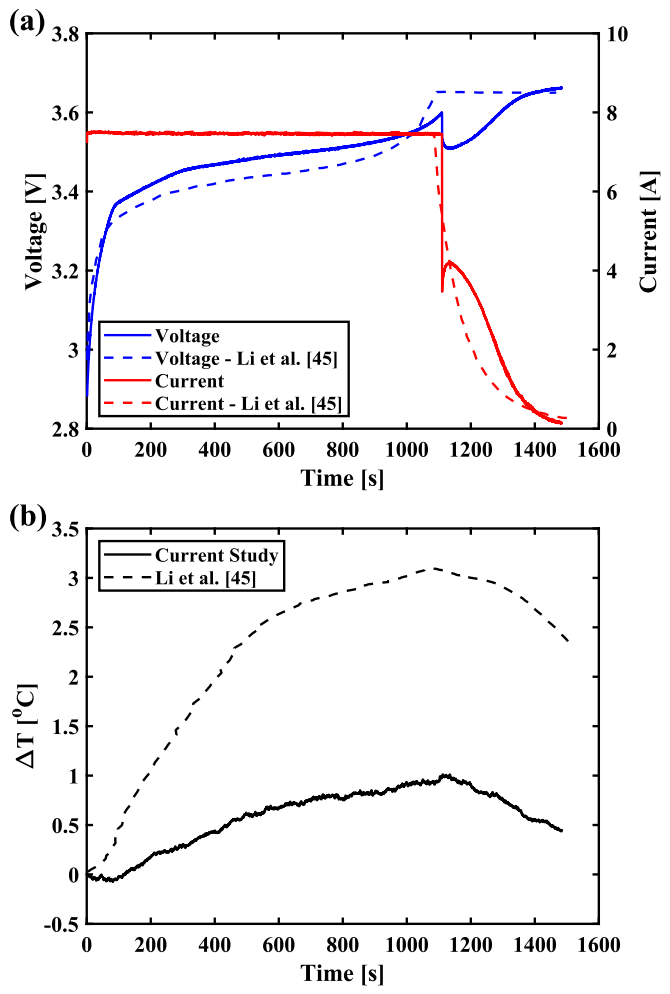

Fig. 8. Comparison with the work of Li et al. [45] for 3C CC-CV charging of the ANR26650M1B cell under preheating immersion conditions, illustrating (a) voltage and current profile and (b) average surface temperature rise.

3.2.2. *Single phase immersion cooling in HFE 7000 and natural convection air cooling*

The average temperature rise of the cell at a charging rate of 1C under preheated immersion cooling conditions in (Novec) HFE 7000 is compared in Fig. 9 to single phase liquid immersion cooling in the same fluid, as well as natural convection air cooling conditions, for initial temperatures of 19 °C and 20 °C respectively. In a similar manner to the discharging performance, greater average surface temperature rises of 1.6 °C and 4.5 °C are determined under single phase liquid immersion and natural convection air cooling conditions respectively when compared to a temperature rise of only 0.3 °C under the preheated immersion case.

3.2.3. *Cell temperature gradient comparisons*

Examining the temperature difference across the cell's axis during charging, excellent thermal homogeneity is observed under preheated immersion conditions with a maximum point-to-point surface temperature difference of approximately 0.3 °C established across the cell for all charging rates investigated. This temperature gradient occurs at the end of the CC stage of the charging process, when the cell's heat generation rate is at its greatest. As the CV stage proceeds, the heat generation rate declines due to the reduced current, leading to a slightly lower temperature difference across the cell at the end of charging of approximately 0.2 °C for all charging rates. Under single phase liquid immersion and natural convection air cooling conditions, maximum temperature differences of 0.3 °C and 0.6 °C are reached respectively at a charging rate of 1C.

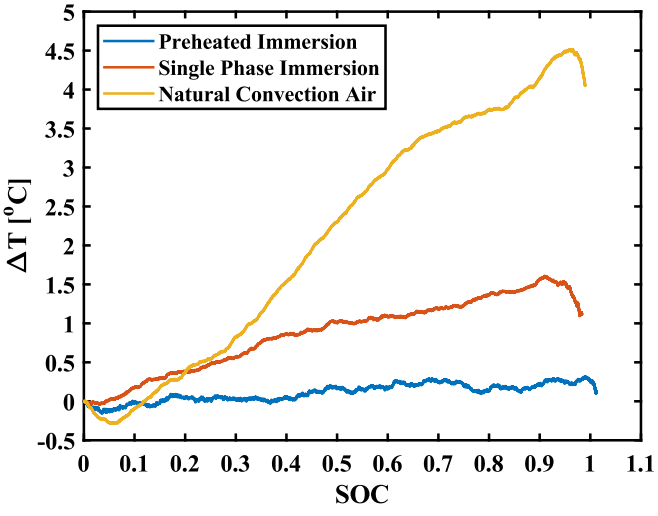

Fig. 9. Temperature rise of the ANR26650M1B cell under preheated immersion, single phase immersion and natural convection air cooling conditions at a charging rate of 1C.

4. Conclusions and future work

The suitability of dielectric liquid immersion cooling for the thermal management of lithium-ion batteries was experimentally investigated in this study for a single 26650 $LiFePO_4$ cylindrical cell completely immersed in the dielectric fluid (Novec) HFE 7000. The thermal and electrical performance of the cell was examined for charging and discharging rates of up to 4C and 10C, respectively, where C can be defined as the measure of the rate at which a cell is charged or discharged relative to its rated capacity.

At a preheated liquid pool temperature of 33 ± 0.5 °C for discharge rates ≥ 2C, subcooled boiling conditions were established as the average surface temperature of the cell exceeded the fluid's saturation temperature of 34 °C, with the change of phase significantly increasing the rate of heat transfer. The generation of vapour bubbles was first observed from the cell's electrodes at the end of 4C discharge. The frequency of their nucleation and departure was noted to increase for greater discharge rates, further enhancing the rate of heat transfer through agitation of the cell's thermal boundary layer. For this cooling method, the cell was maintained within the required operating temperature limits for lithium-ion cells for all discharge rates investigated, with the temperature rise and average cell temperature limited to 3.6 °C and 35.9 °C at the end of 10C discharge, respectively. Additionally, two-phase immersion cooling was shown to provide good thermal homogenisation, with a maximum axial temperature difference of 1 °C across the cell under the most onerous conditions of 10C discharge. Superior performance during discharge was illustrated for two-phase immersion cooling against both single phase liquid immersion in the same liquid and natural convective air cooling under 4C discharge, with temperature rises of 2.1 °C, 6.8 °C and 19 °C respectively. The improved performance offered by immersion cooling was also evident for charging of the cell for rates up to 4C, typically considered as fast charging, with the temperature rise limited to approximately 1 °C and a maximum axial temperature difference across the cell of only 0.3 °C.

Future work will further examine the suitability of immersion cooling for vehicle battery thermal management, including the arrangement of cells within a module, reduction of the fluid volume, as well as the performance of this cooling method under drive cycling conditions which replicate real-world conditions more closely.

Nomenclature

C	cell C rate, 1/h
C_{cell}	cell capacity, Ah
$\frac{dU}{dT}$	entropic heat coefficient, V/K
I	current, A
Q	heat generation rate, W
t	time, s
T	temperature, °C or K
ΔT	temperature difference, °C or K
U	open circuit voltage, V
V	voltage, V

Subscript

avg	average
cell	cell
char	charge
dis	discharge
irr	irreversible
max	maximum
rev	reversible
surf	surface

Greek symbols

η	overpotential, V

Acronyms

BTMS	battery thermal management system
CC	constant current
CV	constant voltage
DOD	depth of discharge
EV	electric vehicle
HEV	hybrid electric vehicle
HFE	hydrofluoroether
ICE	internal combustion engine
LFP	lithium iron phosphate
LTO	lithium titanium oxide
NCA	lithium nickel cobalt aluminium oxide
NMC	lithium nickel manganese cobalt oxide
OCV	open circuit voltage
PCM	phase change material
SEI	solid electrolyte interphase
SOC	state of charge

CRediT authorship contribution statement

N. P. Williams: Conceptualization, Methodology, Investigation, Writing - Original draft preparation, Writing - Review & Editing, Visualization **D. Trimble:** Conceptualization, Methodology, Supervision, Project administration, Funding acquisition, **S. M. O'Shaughnessy:** Conceptualization, Methodology, Writing - Original draft preparation, Writing - Reviewing and Editing, Project administration, Funding acquisition, Supervision.

Declaration of competing interest

The authors declare that they have no known competing financial interests or personal relationships that could have appeared to influence the work reported in this paper.

Data availability

Data will be made available on request.

Acknowledgements

The authors wish to acknowledge the financial support from Trinity College Dublin's Provost's PhD Project Award and the Research Boost Programme, and Science Foundation Ireland (SFI) through the 2050 National Challenge Fund (Award 22/NCF/TF/10952).

References

[1] A.A. Pesaran, Battery thermal models for hybrid vehicle simulations, J. Power Sources 110 (2) (2002) 377–382, https://doi.org/10.1016/S0378-7753(02)00200-8.
[2] C.R. Birkl, M.R. Roberts, E. McTurk, P.G. Bruce, D.A. Howey, Degradation diagnostics for lithium ion cells, J. Power Sources 341 (2017) 373–386, https://doi.org/10.1016/j.jpowsour.2016.12.011.
[3] X. Feng, M. Ouyang, X. Liu, L. Lu, Y. Xia, X. He, Thermal runaway mechanism of lithium ion battery for electric vehicles: a review, Energy Stor. Mater. 10 (2018) 246–267, https://doi.org/10.1016/j.ensm.2017.05.013.
[4] X. Zhao, Y. Yin, Y. Hu, S.Y. Choe, Electrochemical-thermal modeling of lithium plating/stripping of $Li(Ni_{0.6}Mn_{0.2}Co_{0.2})O_2$/carbon lithium-ion batteries at subzero ambient temperatures, J. Power Sources 418 (2019) 61–73, https://doi.org/10.1016/j.jpowsour.2019.02.001.
[5] J. Deng, C. Bae, A. Denlinger, T. Miller, Electric vehicles batteries: requirements and challenges, Joule 4 (3) (2020) 511–515, https://doi.org/10.1016/j.joule.2020.01.013.
[6] A. Tomaszewska, et al., Lithium-ion battery fast charging: a review, eTransportation 1 (2019) 100011, https://doi.org/10.1016/j.etran.2019.100011.
[7] P. Nelson, D. Dees, K. Amine, G. Henriksen, Modeling thermal management of lithium-ion PNGV batteries, J. Power Sources 110 (2) (2002) 349–356, https://doi.org/10.1016/S0378-7753(02)00197-0.
[8] M.S. Wu, K.H. Liu, Y.Y. Wang, C.C. Wan, Heat dissipation design for lithium-ion batteries, J. Power Sources 109 (1) (2002) 160–166, https://doi.org/10.1016/S0378-7753(02)00048-4.
[9] L. Fan, J.M. Khodadadi, A.A. Pesaran, A parametric study on thermal management of an air-cooled lithium-ion battery module for plug-in hybrid electric vehicles, J. Power Sources 238 (2013) 301–312, https://doi.org/10.1016/j.jpowsour.2013.03.050.
[10] S. Park, D. Jung, Battery cell arrangement and heat transfer fluid effects on the parasitic power consumption and the cell temperature distribution in a hybrid electric vehicle, J. Power Sources 227 (2013) 191–198, https://doi.org/10.1016/j.jpowsour.2012.11.039.
[11] H. Sun, R. Dixon, Development of cooling strategy for an air cooled lithium-ion battery pack, J. Power Sources 272 (2014) 404–414, https://doi.org/10.1016/j.jpowsour.2014.08.107.
[12] K. Chen, M. Song, W. Wei, S. Wang, Structure optimization of parallel air-cooled battery thermal management system with U-type flow for cooling efficiency improvement, Energy 145 (2018) 603–613, https://doi.org/10.1016/j.energy.2017.12.110.
[13] K. Chen, S. Wang, M. Song, L. Chen, Structure optimization of parallel air-cooled battery thermal management system, Int. J. Heat Mass Transf. 111 (2017) 943–952, https://doi.org/10.1016/j.ijheatmasstransfer.2017.04.026.
[14] Y. Liu, J. Zhang, Design a J-type air-based battery thermal management system through surrogate-based optimization, Appl. Energy 252 (2019) 113426, https://doi.org/10.1016/j.apenergy.2019.113426.
[15] K. Yu, X. Yang, Y. Cheng, C. Li, Thermal analysis and two-directional air flow thermal management for lithium-ion battery pack, J. Power Sources 270 (2014) 193–200, https://doi.org/10.1016/j.jpowsour.2014.07.086.
[16] R. Mahamud, C. Park, Reciprocating air flow for Li-ion battery thermal management to improve temperature uniformity, J. Power Sources 196 (13) (2011) 5685–5696, https://doi.org/10.1016/j.jpowsour.2011.02.076.
[17] S. Al Hallaj, J.R. Selman, A novel thermal management system for electric vehicle batteries using phase-change material, J. Electrochem. Soc. 147 (9) (2000) 3231–3236, https://doi.org/10.1149/1.1393888.
[18] N. Javani, I. Dincer, G.F. Naterer, B.S. Yilbas, Heat transfer and thermal management with PCMs in a Li-ion battery cell for electric vehicles, Int. J. Heat Mass Transf. 72 (2014) 690–703, https://doi.org/10.1016/j.ijheatmasstransfer.2013.12.076.
[19] S.A. Khateeb, S. Amiruddin, M. Farid, J.R. Selman, S. Al-Hallaj, Thermal management of Li-ion battery with phase change material for electric scooters: experimental validation, J. Power Sources 142 (1–2) (2005) 345–353, https://doi.org/10.1016/j.jpowsour.2004.09.033.
[20] Z. Rao, Y. Huo, X. Liu, G. Zhang, Experimental investigation of battery thermal management system for electric vehicle based on paraffin/copper foam, J. Energy Inst. 88 (3) (2015) 241–246, https://doi.org/10.1016/j.joei.2014.09.006.
[21] Z. Wang, et al., Experimental study of a passive thermal management system for three types of battery using copper foam saturated with phase change materials, RSC Adv. 7 (44) (2017) 27441–27448, https://doi.org/10.1039/C7RA03963H.

[22] W.Q. Li, Z.G. Qu, Y.L. He, Y.B. Tao, Experimental study of a passive thermal management system for high-powered lithium ion batteries using porous metal foam saturated with phase change materials, J. Power Sources 255 (2014) 9–15, https://doi.org/10.1016/j.jpowsour.2014.01.006.
[23] A. Mills, S. Al-Hallaj, Simulation of passive thermal management system for lithium-ion battery packs, J. Power Sources 141 (2) (2005) 307–315, https://doi.org/10.1016/j.jpowsour.2004.09.025.
[24] P. Goli, S. Legedza, A. Dhar, R. Salgado, J. Renteria, A.A. Balandin, Graphene-enhanced hybrid phase change materials for thermal management of Li-ion batteries, J. Power Sources 248 (2014) 37–43, https://doi.org/10.1016/j.jpowsour.2013.08.135.
[25] A. Babapoor, M. Azizi, G. Karimi, Thermal management of a Li-ion battery using carbon fiber-PCM composites, Appl. Therm. Eng. 82 (2015) 281–290, https://doi.org/10.1016/j.applthermaleng.2015.02.068.
[26] Y. Huo, Z. Rao, X. Liu, J. Zhao, Investigation of power battery thermal management by using mini-channel cold plate, Energy Convers. Manag. 89 (2015) 387–395, https://doi.org/10.1016/j.enconman.2014.10.015.
[27] L.W. Jin, P.S. Lee, X.X. Kong, Y. Fan, S.K. Chou, Ultra-thin minichannel LCP for EV battery thermal management, Appl. Energy 113 (2014) 1786–1794, https://doi.org/10.1016/j.apenergy.2013.07.013.
[28] M. Malik, I. Dincer, M.A. Rosen, M. Mathew, M. Fowler, Thermal and electrical performance evaluations of series connected Li-ion batteries in a pack with liquid cooling, Appl. Therm. Eng. 129 (2018) 472–481, https://doi.org/10.1016/j.applthermaleng.2017.10.029.
[29] M. Pan, X. Zhong, G. Dong, P. Huang, Experimental study of the heat dissipation of battery with a manifold micro-channel heat sink, Appl. Therm. Eng. 163 (2019) 114330, https://doi.org/10.1016/j.applthermaleng.2019.114330.
[30] Z. Rao, X. Zhang, Investigation on thermal management performance of wedge-shaped microchannels for rectangular Li-ion batteries, Int. J. Energy Res. 43 (8) (2019) 3876–3890, https://doi.org/10.1002/er.4571.
[31] M.S. Patil, J.H. Seo, S. Panchal, S.W. Jee, M.Y. Lee, Investigation on thermal performance of water-cooled Li-ion pouch cell and pack at high discharge rate with U-turn type microchannel cold plate, Int. J. Heat Mass Transf. 155 (2020) 119728, https://doi.org/10.1016/j.ijheatmasstransfer.2020.119728.
[32] L. Wei, L. Jia, Z. An, C. Dang, Experimental study on thermal management of cylindrical Li-ion battery with flexible microchannel plates, J. Therm. Sci. 29 (4) (2020) 1001–1009, https://doi.org/10.1007/s11630-020-1331-1.
[33] Z. An, L. Jia, X. Li, Y. Ding, Experimental investigation on lithium-ion battery thermal management based on flow boiling in mini-channel, Appl. Therm. Eng. 117 (2017) 534–543, https://doi.org/10.1016/j.applthermaleng.2017.02.053.
[34] S.H. Hong, D.S. Jang, S. Park, S. Yun, Y. Kim, Thermal performance of direct two-phase refrigerant cooling for lithium-ion batteries in electric vehicles, Appl. Therm. Eng. 173 (2020) 115213, https://doi.org/10.1016/j.applthermaleng.2020.115213.
[35] Z. Rao, Y. Huo, X. Liu, Experimental study of an OHP-cooled thermal management system for electric vehicle power battery, Exp. Thermal Fluid Sci. 57 (2014) 20–26, https://doi.org/10.1016/j.expthermflusci.2014.03.017.
[36] K. Chen, X. Li, Accurate determination of battery discharge characteristics – a comparison between two battery temperature control methods, J. Power Sources 247 (2014) 961–966, https://doi.org/10.1016/j.jpowsour.2013.09.060.
[37] D.W. Sundin, S. Sponholtz, Thermal management of Li-ion batteries with single-phase liquid immersion cooling, IEEE Open J. Veh. Technol. 1 (2020) 82–92, https://doi.org/10.1109/OJVT.2020.2972541.
[38] M. Suresh Patil, J.H. Seo, M.Y. Lee, A novel dielectric fluid immersion cooling technology for Li-ion battery thermal management, Energy Convers. Manag. 229 (2021) 113715, https://doi.org/10.1016/j.enconman.2020.113715.
[39] Y. Li, Z. Zhou, W.T. Wu, Three-dimensional thermal modeling of Li-ion battery cell and 50 V Li-ion battery pack cooled by mini-channel cold plate, Appl. Therm. Eng. 147 (2019) 829–840, https://doi.org/10.1016/j.applthermaleng.2018.11.009.
[40] H. Wang, T. Tao, J. Xu, H. Shi, X. Mei, P. Gou, Thermal performance of a liquid-immersed battery thermal management system for lithium-ion pouch batteries, J. Energy Storage 46 (2022) 103835, https://doi.org/10.1016/j.est.2021.103835.
[41] H. Hirano, T. Tajima, T. Hasegawa, T. Sekiguchi, M. Uchino, Boiling liquid battery cooling for electric vehicle, in: 2014 IEEE Conference and Expo Transportation Electrification Asia-Pacific (ITEC Asia-Pacific), Beijing, China, 2014, pp. 1–4, https://doi.org/10.1109/ITEC-AP.2014.6940931.
[42] R.W. van Gils, D. Danilov, P.H.L. Notten, M.F.M. Speetjens, H. Nijmeijer, Battery thermal management by boiling heat-transfer, Energy Convers. Manag. 79 (2014) 9–17, https://doi.org/10.1016/j.enconman.2013.12.006.
[43] L. Giammichele, V. D'Alessandro, M. Falone, R. Ricci, Experimental study of a direct immersion liquid cooling of a Li-ion battery for electric vehicles applications, Int. J. Heat Technol. 40 (1) (2022) 1–8, https://doi.org/10.18280/ijht.400101.
[44] Y. Li, et al., Experimental studies of liquid immersion cooling for 18650 lithium-ion battery under different discharging conditions, Case Stud. Therm. Eng. 34 (2022) 102034, https://doi.org/10.1016/j.csite.2022.102034.
[45] Y. Li, et al., Experimental study of liquid immersion cooling for different cylindrical lithium-ion batteries under rapid charging conditions, Therm. Sci. Eng. Prog. 37 (2023) 101569, https://doi.org/10.1016/j.tsep.2022.101569.
[46] L. Giammichele, V. D'Alessandro, M. Falone, R. Ricci, Preliminary analysis of a novel battery thermal management system based on a low boiling dielectric fluid, IOP Conf. Ser.: Earth Environ. Sci. 1106 (1) (2022) 012017, https://doi.org/10.1088/1755-1315/1106/1/012017.
[47] Y.F. Wang, J.T. Wu, Thermal performance predictions for an HFE-7000 direct flow boiling cooled battery thermal management system for electric vehicles, Energy Convers. Manag. 207 (2020) 112569, https://doi.org/10.1016/j.enconman.2020.112569.
[48] N. Wu, X. Ye, J. Yao, X. Zhang, X. Zhou, B. Yu, Efficient thermal management of the large-format pouch lithium-ion cell via the boiling-cooling system operated with intermittent flow, Int. J. Heat Mass Transf. 170 (2021) 121018, https://doi.org/10.1016/j.ijheatmasstransfer.2021.121018.
[49] M. Al-Zareer, I. Dincer, M.A. Rosen, A novel approach for performance improvement of liquid to vapor based battery cooling systems, Energy Convers. Manag. 187 (2019) 191–204, https://doi.org/10.1016/j.enconman.2019.02.063.
[50] M. Al-Zareer, I. Dincer, M.A. Rosen, Electrochemical modeling and performance evaluation of a new ammonia-based battery thermal management system for electric and hybrid electric vehicles, Electrochim. Acta 247 (2017) 171–182, https://doi.org/10.1016/j.electacta.2017.06.162.
[51] M. Al-Zareer, I. Dincer, M.A. Rosen, Development and evaluation of a new ammonia boiling based battery thermal management system, Electrochim. Acta 280 (2018) 340–352, https://doi.org/10.1016/j.electacta.2018.05.093.
[52] M. Al-Zareer, I. Dincer, M.A. Rosen, Heat and mass transfer modeling and assessment of a new battery cooling system, Int. J. Heat Mass Transf. 126 (2018) 765–778, https://doi.org/10.1016/j.ijheatmasstransfer.2018.04.157.
[53] M. Doyle, J. Newman, A.S. Gozdz, C.N. Schmutz, J.M. Tarascon, Comparison of modeling predictions with experimental data from plastic lithium ion cells, J. Electrochem. Soc. 143 (6) (1996) 1890–1903, https://doi.org/10.1149/1.1836921.
[54] H. Zhou, C. Dai, Y. Liu, X. Fu, Y. Du, Experimental investigation of battery thermal management and safety with heat pipe and immersion phase change liquid, J. Power Sources 473 (2020) 228545, https://doi.org/10.1016/j.jpowsour.2020.228545.
[55] Y. Li, et al., Experimental investigations of liquid immersion cooling for 18650 lithium-ion battery pack under fast charging conditions, Appl. Therm. Eng. 227 (2023) 120287, https://doi.org/10.1016/j.applthermaleng.2023.120287.
[56] J.W. Han, K.S. Garud, S.G. Hwang, M.Y. Lee, Experimental study on dielectric fluid immersion cooling for thermal management of lithium-ion battery, Symmetry 14 (2022) 2126, https://doi.org/10.3390/sym14102126.
[57] E. Solai, M. Guadagnini, H. Beaugendre, R. Daccord, P. Congedo, Validation of a data-driven fast numerical model to simulate the immersion cooling of a lithium-ion battery pack, Energy 249 (2022) 123633, https://doi.org/10.1016/j.energy.2022.123633.
[58] L. Giammichele, V. D'Alessandro, M. Falone, R. Ricci, Thermal behaviour assessment and electrical characterisation of a cylindrical Lithium-ion battery using infrared thermography, Appl. Therm. Eng. 205 (2022) 117974, https://doi.org/10.1016/j.applthermaleng.2021.117974.
[59] M. Xu, R. Wang, B. Reichman, X. Wang, Modeling the effect of two-stage fast charging protocol on thermal behavior and charging energy efficiency of lithium-ion batteries, J. Energy Storage 20 (2018) 298–309, https://doi.org/10.1016/j.est.2018.09.004.
[60] S.J. Drake, D.A. Wetz, J.K. Ostanek, S.P. Miller, J.M. Heinzel, Measurement of anisotropic thermophysical properties of cylindrical Li-ion cells, J. Power Sources 252 (2014) 298–304, https://doi.org/10.1016/j.jpowsour.2013.11.107.
[61] D. Bernardi, E. Pawlikowski, J. Newman, A general energy balance for battery systems, J. Electrochem. Soc. 132 (1) (1985) 5–12, https://doi.org/10.1149/1.2113792.
[62] T.M. Bandhauer, S. Garimella, T.F. Fuller, A critical review of thermal issues in lithium-ion batteries, J. Electrochem. Soc. 158 (3) (2011) R1–R25, https://doi.org/10.1149/1.3515880.
[63] H.W. Coleman, W.G. Steele, Experimentation, Validation, and Uncertainty Analysis for Engineers, John Wiley & Sons, Inc., New Jersey, USA, 2009.
[64] LithiumWerks, 26650 Lithium Ion Power Cell, 2022.
[65] A. Hausmann, C. Depcik, Expanding the Peukert equation for battery capacity modeling through inclusion of a temperature dependency, J. Power Sources 235 (2013) 148–158, https://doi.org/10.1016/j.jpowsour.2013.01.174.
[66] J. Chiew, C.S. Chin, W.D. Toh, Z. Gao, J. Jia, C.Z. Zhang, A pseudo three-dimensional electrochemical-thermal model of a cylindrical $LiFePO_4$/graphite battery, Appl. Therm. Eng. 147 (2019) 450–463, https://doi.org/10.1016/j.applthermaleng.2018.10.108.
[67] J. Weng, D. Ouyang, X. Yang, M. Chen, G. Zheng, J. Wang, Optimization of the internal fin in a phase-change-material module for battery thermal management, Appl. Therm. Eng. 167 (2020) 114698, https://doi.org/10.1016/j.applthermaleng.2019.114698.
[68] G. Jiang, J. Huang, Y. Fu, M. Cao, M. Liu, Thermal optimization of composite phase change material/expanded graphite for Li-ion battery thermal management, Appl. Therm. Eng. 108 (2016) 1119–1125, https://doi.org/10.1016/j.applthermaleng.2016.07.197.
[69] J. Chiew, C.S. Chin, J.B. Jia, W.D. Toh, Thermal analysis of a latent heat storage based battery thermal cooling wrap, in: Proceedings of the 2017 COMSOL Conference — Call for Papers and Posters, (Singapore) vol. 9, 2017 [Online]. Available: https://www.comsol.com/paper/thermal-analysis-of-a-latent-heat-storage-based-battery-thermal-cooling-wrap-60123.
[70] K. Li, J. Yan, Y. Fu, H. Chen, Q. Wang, Water cooling based strategy for lithium ion battery pack dynamic cycling for thermal management system, Appl. Therm. Eng. 132 (2018) 575–585, https://doi.org/10.1016/j.applthermaleng.2017.12.131.
[71] C. Forgez, D. Vinh Do, G. Friedrich, M. Morcrette, C. Delacourt, Thermal modeling of a cylindrical $LiFePO_4$/graphite lithium-ion battery, J. Power Sources 195 (9) (2010) 2961–2968, https://doi.org/10.1016/j.jpowsour.2009.10.105.